SUPPORTING INFORMATION

Electronic Origin of Oxygen Transport Behavior in La-Based Perovskites: A Density Functional Theory Study

Ya-Shan Zheng,[a] *Min Zhang,*[a] *Qian Li,*[a] *Yi-An Zhu,*[a,*] *Zhi-Jun Sui,*[a] *De Chen,*[b] *Xing-Gui Zhou*[a]

[a]UNILAB, State Key Laboratory of Chemical Engineering, Shanghai Key Laboratory of Multiphase Materials Chemical Engineering, East China University of Science and Technology, Shanghai 200237, China

[b]Department of Chemical Engineering, Norwegian University of Science and Technology, N-7491 Trondheim, Norway

[*]Corresponding author. Tel: +86 21 6425 3072; Fax: +86 21 6425 3528

Email: yanzhu@ecust.edu.cn

1. Computational details

The electronic, magnetic, and crystal structures of $LaMO_3$ (M = Sc - Cu) perovskites used in the calculation are summarized in Table S1.

Table S1. Electronic, magnetic, and crystal structures of $LaMO_3$ (M = Sc - Cu) perovskites.

Perovskite	PAW potential		U_{eff} in PBE+U	U_{eff} in BEEF-vdW+U	Magnetic structure	Crystal structure (Orthorhombic & Rhombohedral)
$LaScO_3$	La O_s	Sc_sv	0	0	NM[a]	*Pbnm*
$LaTiO_3$		Ti_pv	1.3	0.6	GAFM[b]	*Pbnm*
$LaVO_3$		V_sv	3.0	2.5	CAFM[c]	*Pbnm*
$LaCrO_3$		Cr_pv	3.0	2.5	GAFM	*Pbnm*
$LaMnO_3$		Mn_pv	4.7	3.5	AAFM[d]	*Pbnm*
$LaFeO_3$		Fe_pv	4.8	2.9	GAFM	*Pbnm*
$LaCoO_3$		Co	4.2	3.1	FM[e]	$R\bar{3}c$
$LaNiO_3$		Ni_pv	7.0	5.6	FM	$R\bar{3}c$
$LaCuO_3$		Cu	4.5	2.8	NM	$R\bar{3}c$

[a]Nonemagnetic

[b]G type-antiferromagnetic

[c]C type-antiferromagnetic

[d]A type-antiferromagnetic

[e]Ferromagnetic

2. Determination of U_{eff} value

The U_{eff} (U_{eff} = U - J) values used in this work were obtained by fitting the calculated thermodynamic quantities, such as enthalpy and Gibbs free energy of formation of metal oxides, to available experimental data.

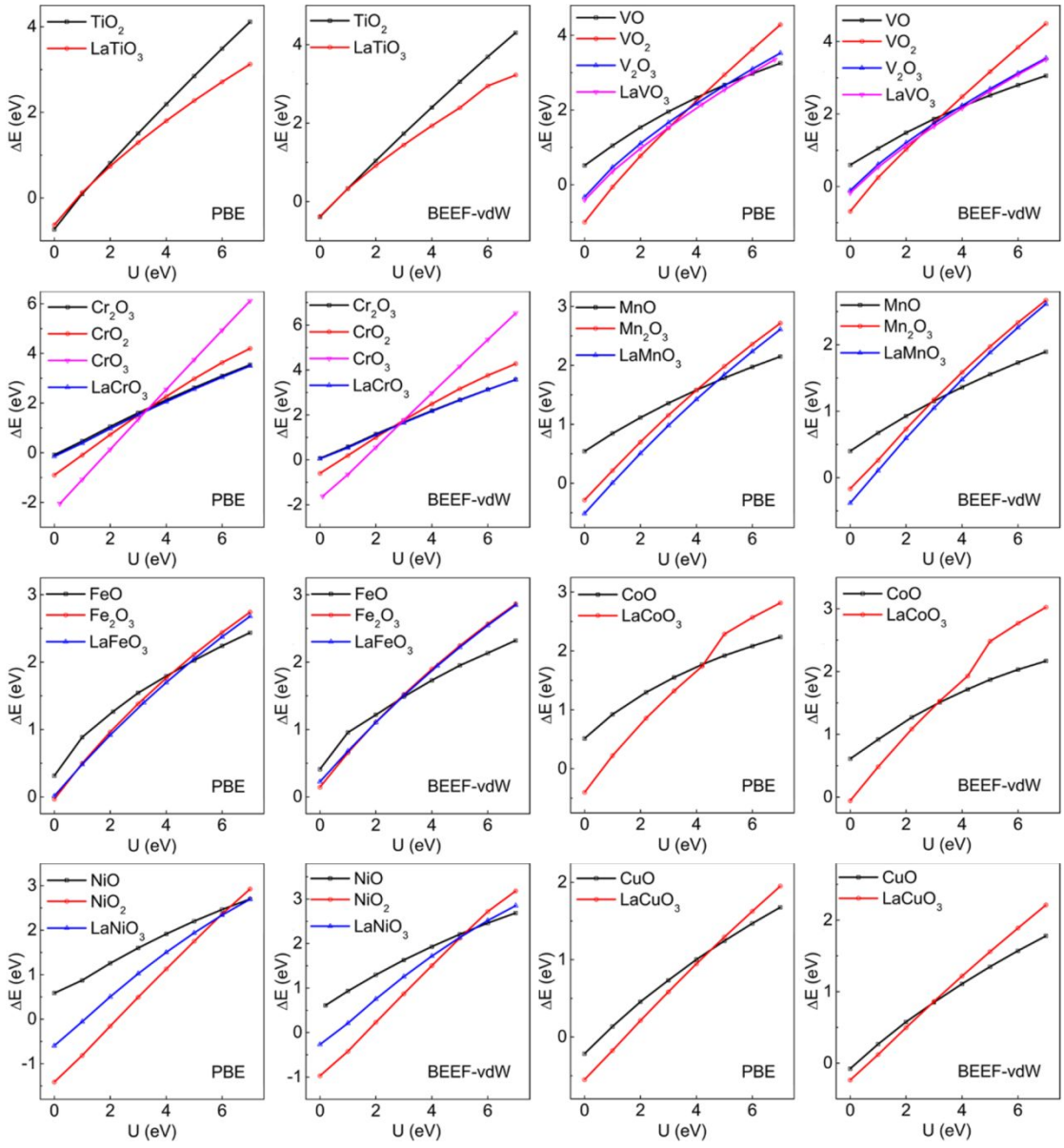

Figure S1. Derivation of the U_{eff} value by using the PBE and the BEEF-vdW functionals.

To ensure that the fitting to the thermodynamic properties can correctly reproduce other physical properties of $LaMO_3$, we calculated the band structures, band gaps, as well as magnetic moments of $LaMO_3$ (M = Sc - Cu) by using the BEEF-vdW+U method, as shown in Figs. S2 and S3,

respectively. Comparison between our calculated band gaps and magnetic moments with experimental data[1-20] and theoretical results reported by using the HSE hybrid functional[21-26] indicates that our fitted U_{eff} values work surprisingly well when determining the physical properties of $LaMO_3$, and, in some cases, BEEF-vdW+U may give even better agreement than the HSE hybrid functional does. The only exception occurs in $LaScO_3$, whose band gap is considerably underestimated. This deviation can be traced to the underestimation of the Sc 3*d* unoccupied band energy, and the calculated error can only be corrected by using a large and unreasonable U_{eff} value because the U_{eff} within the GGA+U framework has a negligible effect on the energy of the unoccupied *d* state. Hence, in this work, BEEF-vdW+U was applied to the La-based perovskites involving 3*d*-block transition metals except $LaScO_3$.

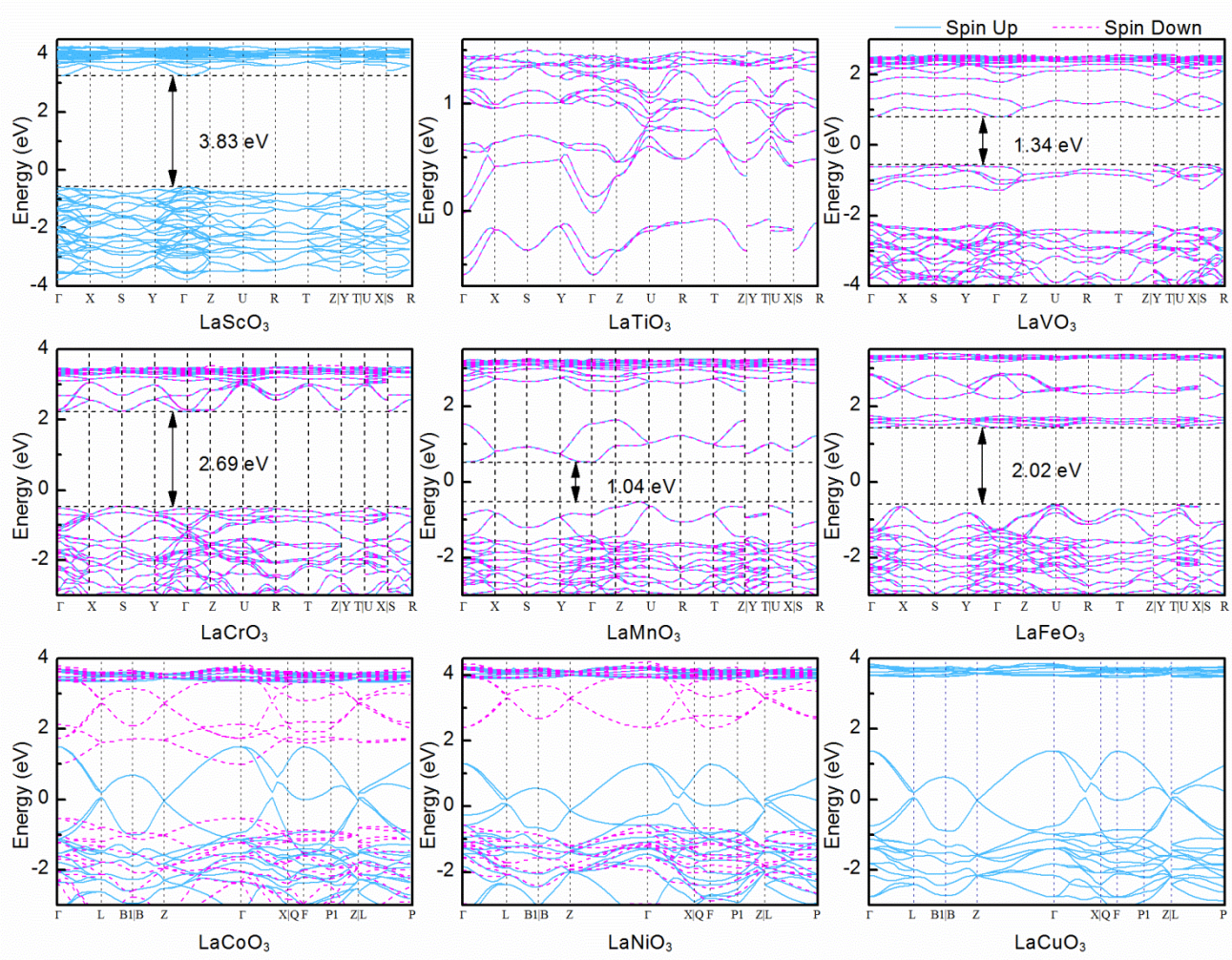

Figure S2. Calculated band structures of $LaMO_3$ (M = Sc - Fe) by BEEF-vdW+U.

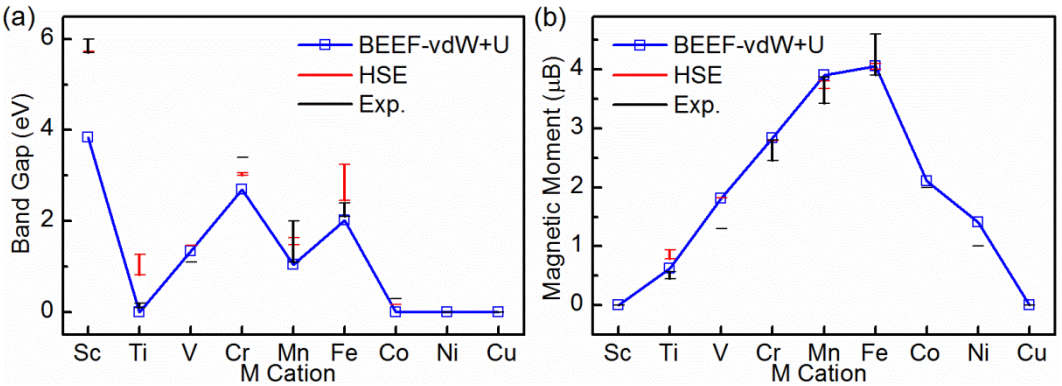

Figure S3. Calculated (a) band gap and (b) magnetic moment of La-based perovskites $LaMO_3$ (M = Sc - Fe) by BEEF-vdW+U. Experimental results reported in ref. 1-20 and theoretical data reported by using the HSE hybrid functional in ref. 21-26 are presented for comparison.

3. Structure distortion

Structural determinations carried out at room temperature suggested that there are multiple ways in which the octahedra can tilt. Very often perovskites would undergo an $a^-a^-a^-$ or an $a^-b^+a^-$ octahedral tilting distortion, with the symmetry reducing from cubic to rhombohedral or to orthorhombic, which can be seen from Fig. S4.

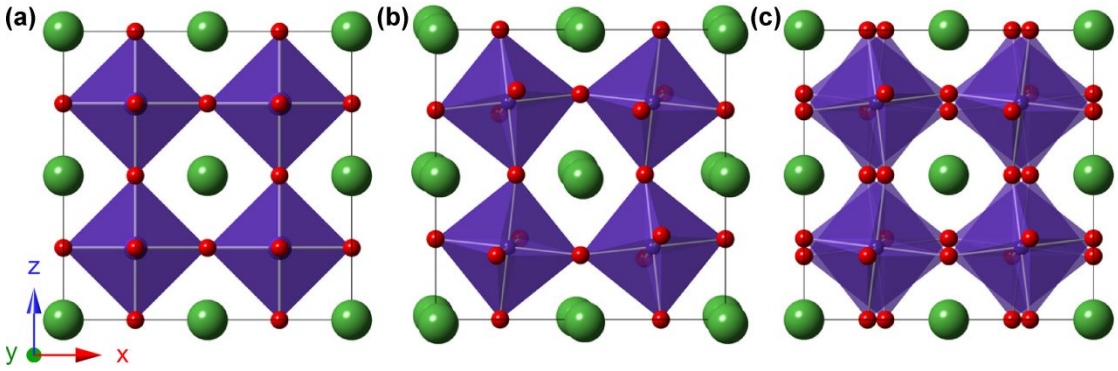

Figure S4. Schematical representations of (a) ideal cubic structure, (b) pseudocubic structure adopting the $a^-b^+a^-$ tilt system, and (c) pseudocubic structure adopting the $a^-a^-a^-$ tilt system.

4.Cell parameters of pseudocubic structures of $LaMO_3$

Pseudocubic structures were obtained by imposing an $a^-b^+a^-$ or an $a^-a^-a^-$ octahedral tilting distortions on the cubic supercells and allowing for internal atomic relaxation. The equilibrium supercell parameters of the pseudocubic structures were obtained by first performing a series of constant-volume calculations and then fitting the energy *vs*. volume data to the Murnaghan equation of state (see Fig. S5). Our calculated results indicate that the pseudocubic model in the $a^-b^+a^-$ tilt system is energetically more favorable than that in the $a^-a^-a^-$ tilt system. Therefore, the $a^-b^+a^-$ octahedral tilting distortion was adopted by all the pseudocubic structures of La-based perovskites.

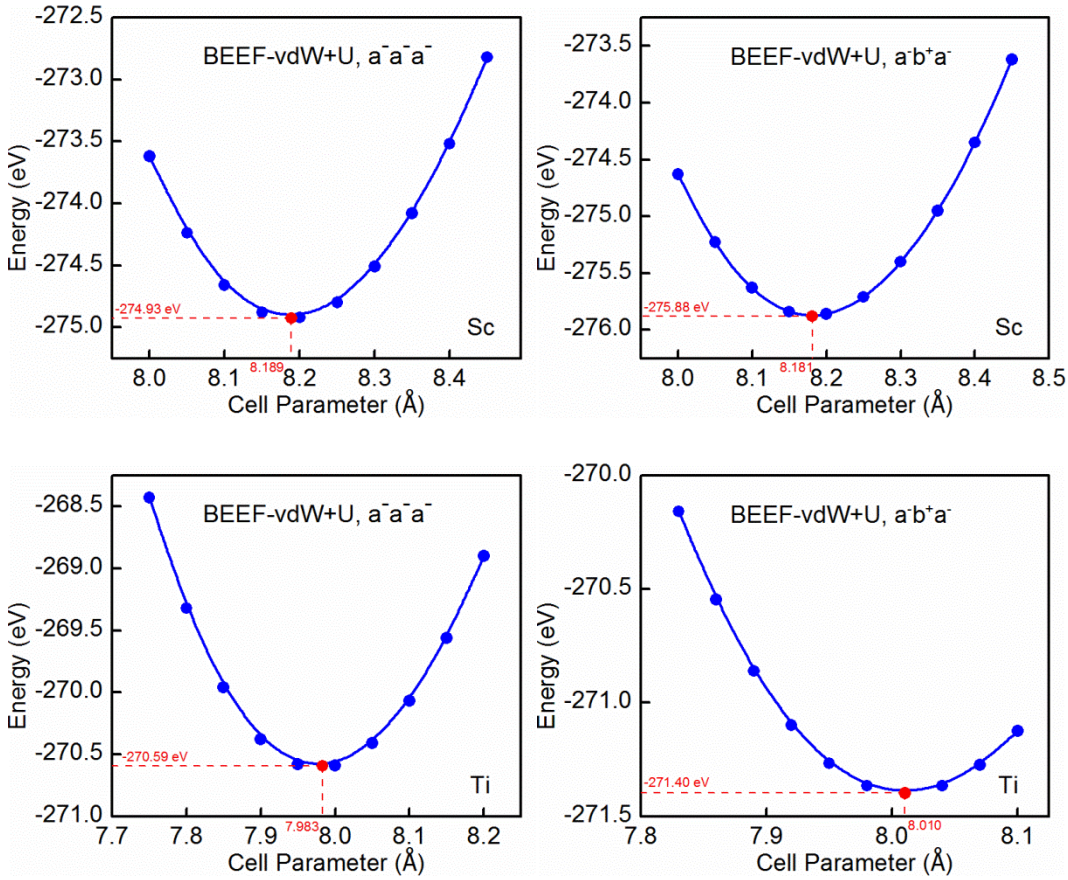

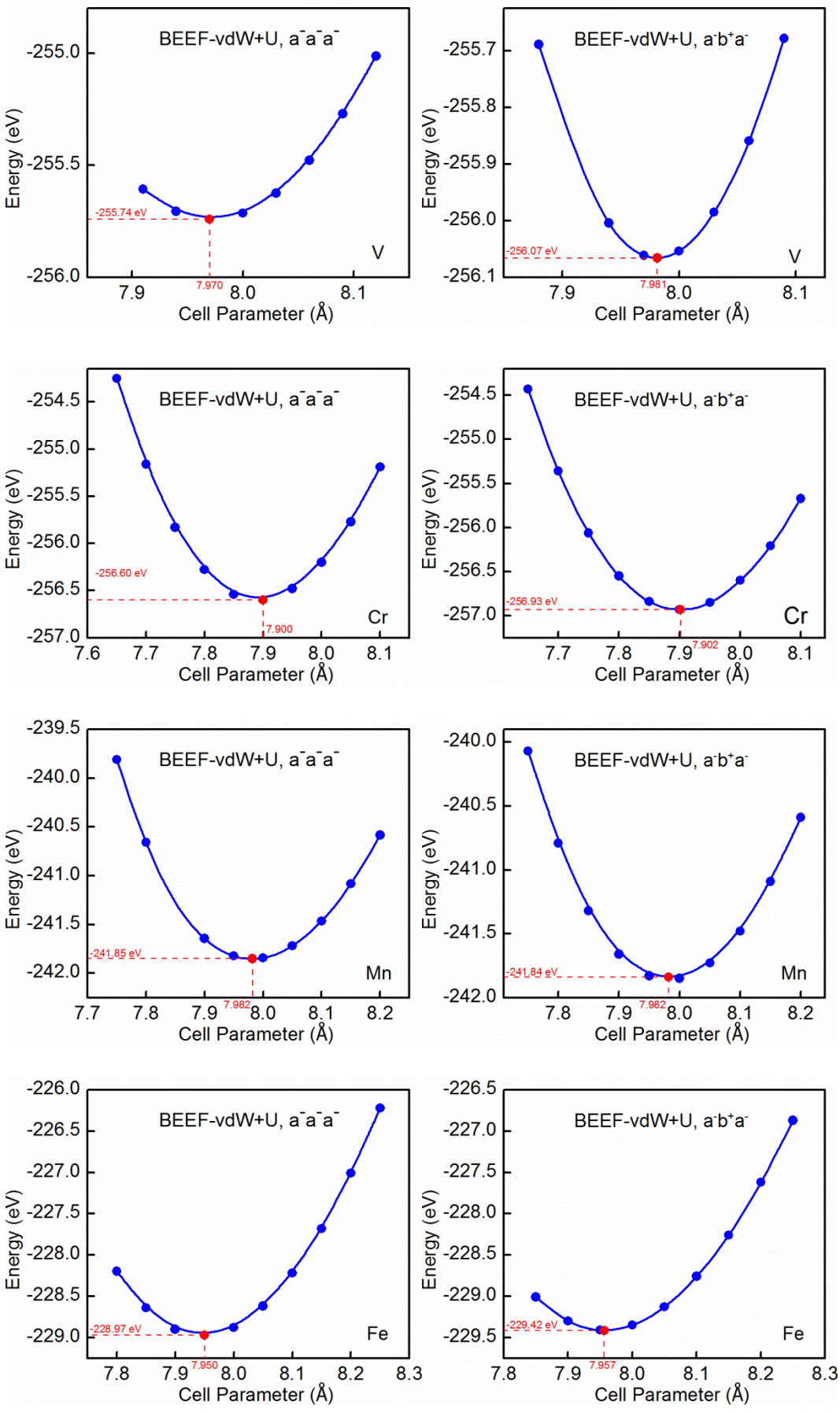
BEEF-vdW+U, a⁻a⁻a⁻
Energy (eV)
Cell Parameter (Å)
-255.74 eV
7.970
V
BEEF-vdW+U, a⁻b⁺a⁻
-256.07 eV
7.981
V
BEEF-vdW+U, a⁻a⁻a⁻
-256.60 eV
7.900
Cr
BEEF-vdW+U, a⁻b⁺a⁻
-256.93 eV
7.902
Cr
BEEF-vdW+U, a⁻a⁻a⁻
-241.85 eV
7.982
Mn
BEEF-vdW+U, a⁻b⁺a⁻
-241.84 eV
7.982
Mn
BEEF-vdW+U, a⁻a⁻a⁻
-228.97 eV
7.950
Fe
BEEF-vdW+U, a⁻b⁺a⁻
-229.42 eV
7.957
Fe

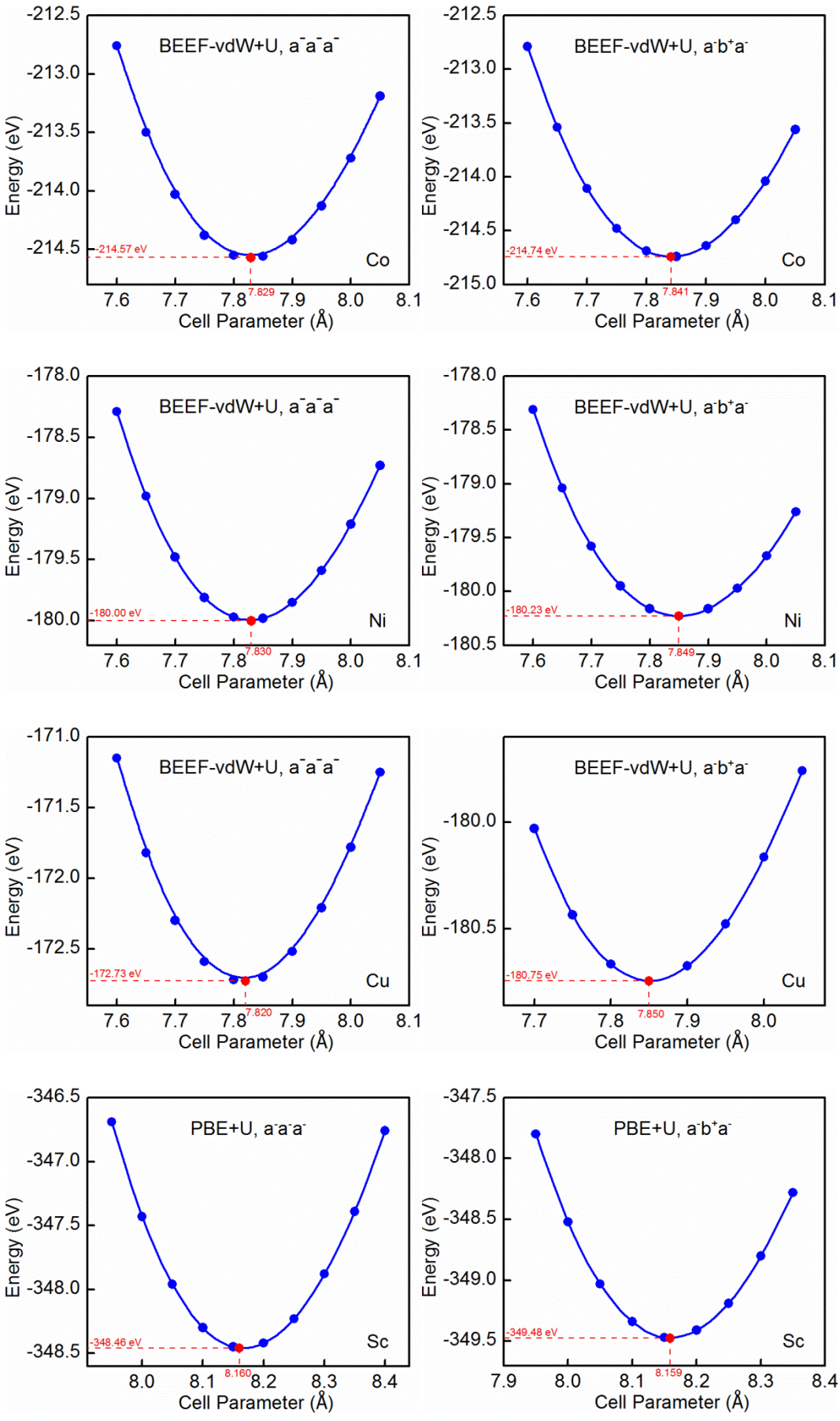
BEEF-vdW+U, a⁻a⁻a⁻
Energy (eV)
Cell Parameter (Å)
-214.57 eV
7.829
Co
BEEF-vdW+U, a⁻b⁺a⁻
-214.74 eV
7.841
Co
BEEF-vdW+U, a⁻a⁻a⁻
-180.00 eV
7.830
Ni
BEEF-vdW+U, a⁻b⁺a⁻
-180.23 eV
7.849
Ni
BEEF-vdW+U, a⁻a⁻a⁻
-172.73 eV
7.820
Cu
BEEF-vdW+U, a⁻b⁺a⁻
-180.75 eV
7.850
Cu
PBE+U, a⁻a⁻a⁻
-348.46 eV
8.160
Sc
PBE+U, a⁻b⁺a⁻
-349.48 eV
8.159
Sc

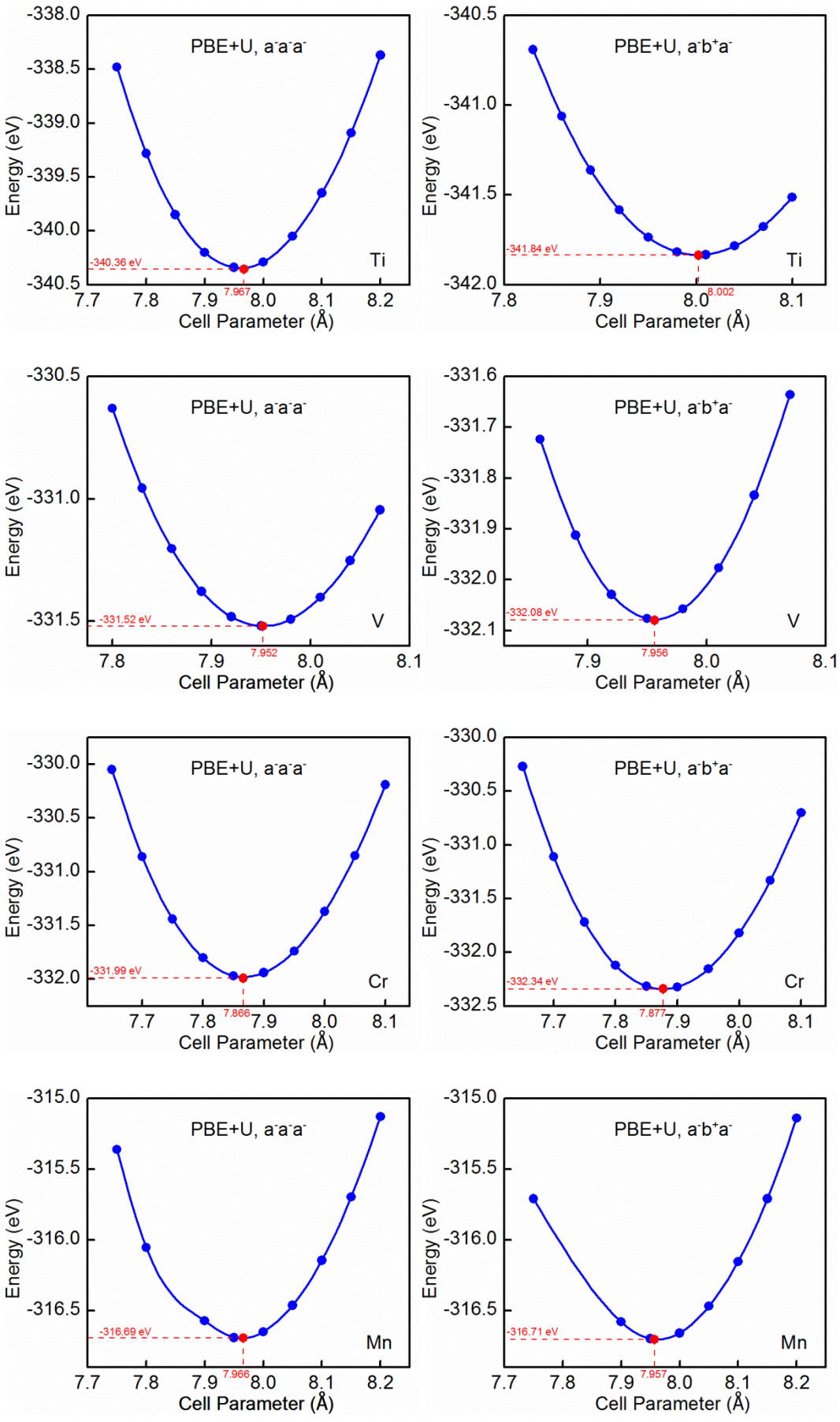
PBE+U, a⁻a⁻a⁻
Ti
-340.36 eV
7.967
PBE+U, a⁻b⁺a⁻
Ti
-341.84 eV
8.002
PBE+U, a⁻a⁻a⁻
V
-331.52 eV
7.952
PBE+U, a⁻b⁺a⁻
V
-332.08 eV
7.956
PBE+U, a⁻a⁻a⁻
Cr
-331.99 eV
7.866
PBE+U, a⁻b⁺a⁻
Cr
-332.34 eV
7.877
PBE+U, a⁻a⁻a⁻
Mn
-316.69 eV
7.966
PBE+U, a⁻b⁺a⁻
Mn
-316.71 eV
7.957
Energy (eV)
Cell Parameter (Å)

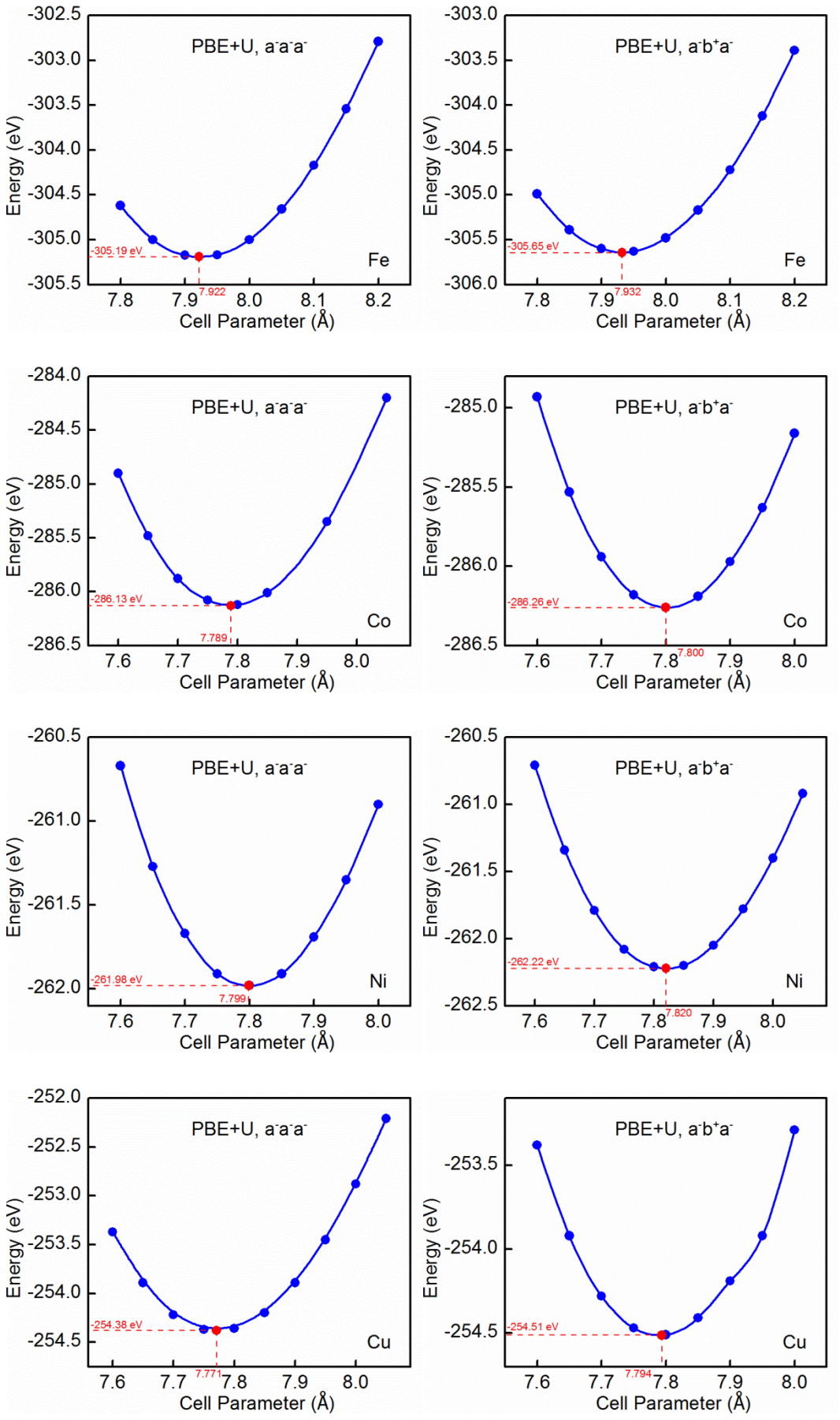

Figure S5. Determination of the cell parameters of pseudocubic structures of $LaMO_3$.

5. O_2 binding energy correction

The calculated and experimental enthalpy and Gibbs free energy of formation of nontransition-metal oxides are compared and presented in Fig. S6, from which the corrections to the O_2 total energy are determined.

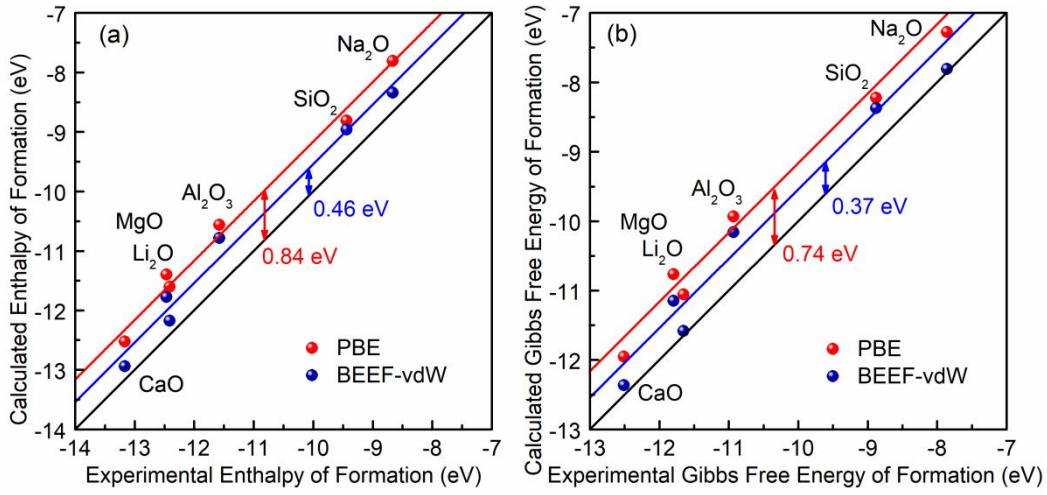

Figure S6. Plots of calculated (a) enthalpy and (b) Gibbs free energy of formation of non-transition metal oxides (*per* mole O_2 at 298 K) against experimental value.

6. Variation in the M-O_C-M bond angle

The octahedral rotation is commonly referred to as $GdFeO_3$-type distortion (or simply GFO distortion) and would considerably decrease the M-O_C-M bond angles from 180°, as summarized in Table S2.

Table S2. Measured M-*Oc*-M bond angles in $LaMO_3$.

Perovskites	M-O_c-M (Å)			
	BEEF-vdW+U		PBE+U	
	Pseudocubic	Orthorhombic & Rhombohedral	Pseudocubic	Orthorhombic & Rhombohedral
$LaScO_3$	146.684	146.143	145.998	146.018
$LaTiO_3$	154.357	153.828	152.486	152.018
$LaVO_3$	151.664	152.424	151.481	151.803
$LaCrO_3$	155.499	155.196	154.838	154.702
$LaMnO_3$	152.155	151.241	151.983	150.840
$LaFeO_3$	153.606	153.749	153.164	153.331
$LaCoO_3$	157.668	159.445	157.604	159.949
$LaNiO_3$	157.272	158.891	157.076	158.757
$LaCuO_3$	158.206	160.384	161.816	161.640

7. Oxygen vacancy formation energy

The calculated oxygen vacancy formation energies in the three perovskite crystal structures by using the BEEF-vdW+U and PBE+U methods are presented in Table S3.

Table S3. Calculated oxygen vacancy formation energies in the three perovskite crystal structures by using the BEEF-vdW+U and PBE+U methods.

Perovskites	BEEF-vdW+U				PBE+U			
	Pseudocubic		Orthorhombic & Rhombohedral		Pseudocubic		Orthorhombic & Rhombohedral	
	O_{ab}	O_c	O_{ab}	O_c	O_{ab}	O_c	O_{ab}	O_c
$LaScO_3$	7.07	7.08	7.10	7.10	7.10	7.11	7.12	7.13
$LaTiO_3$	6.50	6.47	6.52	6.44	6.61	6.63	6.61	6.57
$LaVO_3$	6.05	6.14	6.10	6.29	6.26	6.36	6.21	6.36
$LaCrO_3$	5.49	5.51	5.42	5.48	5.61	5.62	5.54	5.59
$LaMnO_3$	3.37	3.45	4.01	3.96	3.37	3.47	3.96	3.95
$LaFeO_3$	4.77	4.81	4.74	4.76	4.90	4.94	4.79	4.89
$LaCoO_3$	2.23	2.30	2.35		2.12	2.21	2.48	
$LaNiO_3$	1.54	1.59	1.49		1.50	1.55	1.44	
$LaCuO_3$	1.36	1.43	1.16		1.19	1.25	1.14	

From Table S3, one can see that in the orthorhombic and pseudocubic $LaMO_3$ the calculated oxygen vacancy formation energies at the O_{ab} and O_c sites are virtually the same (the difference is less than 0.1 eV), implying that the oxygen vacancies are likely to be distributed uniformly in bulk perovskite. The only exception to this observation is $LaVO_3$, where the energy difference could be as high as 0.19 eV. The origin of the energy difference probably lies in the fact that $LaVO_3$ adopts a C-type antiferromagnetic structure and undergoes a significant GFO distortion in the *c* direction compared to the other perovskite materials, which is reflected in the dramatic reduction of the V-O_c-V bond angle from 180° (see Table S2 for details). As a consequence, the local magnetic and coordination environments of the O_{ab} and O_c ions differ significantly, which in turn gives rise to the markedly different V-O bond strengths.

8. Effective Bader charge on ions in stoichiometric perovskites

The calculated effective Bader charges on La (q_{La}), M (q_M), and O (q_O) in the stoichiometric $LaMO_3$ are presented in Table S4.

Table S4. Bader charge on different ions in stoichiometric perovskites.

Perovskites	BEEF-vdW+U						PBE+U					
	Pseudocubic			Orthorhombic & Rhombohedral			Pseudocubic			Orthorhombic & Rhombohedral		
	q_{La}/(|e|)	q_M/(|e|)	q_O/(|e|)	q_{La}/(|e|)	q_M/(|e|)	q_O/(|e|)	q_{La}/(|e|)	q_M/(|e|)	q_O/(|e|)	q_{La}/(|e|)	q_M/(|e|)	q_O/(|e|)
$LaScO_3$	2.08+	2.02+	1.37-	2.08+	2.02+	1.36-	2.06+	2.00+	1.35-	2.05+	2.00+	1.35-
$LaTiO_3$	2.04+	1.95+	1.33-	2.04+	1.95+	1.33-	2.03+	1.95+	1.33-	2.03+	1.95+	1.32-
$LaVO_3$	2.09+	1.89+	1.33-	2.09+	1.89+	1.33-	2.07+	1.88+	1.32-	2.07+	1.89+	1.32-
$LaCrO_3$	2.10+	1.77+	1.29-	2.10+	1.77+	1.29-	2.08+	1.76+	1.28-	2.08+	1.76+	1.28-
$LaMnO_3$	2.10+	1.72+	1.27-	2.11+	1.72+	1.28-	2.08+	1.72+	1.27-	2.09+	1.72+	1.27-
$LaFeO_3$	2.11+	1.74+	1.28-	2.10+	1.74+	1.28-	2.08+	1.78+	1.29-	2.08+	1.78+	1.29-
$LaCoO_3$	2.12+	1.39+	1.17-	2.11+	1.38+	1.17-	2.10+	1.37+	1.16-	2.10+	1.34+	1.15-
$LaNiO_3$	2.12+	1.33+	1.15-	2.12+	1.33+	1.15-	2.10+	1.33+	1.14-	2.10+	1.33+	1.14-
$LaCuO_3$	2.13+	1.18+	1.10-	2.13+	1.18+	1.10-	2.11+	1.15+	1.09-	2.11+	1.15+	1.09-

9. Charge redistribution in perovskites upon oxygen vacancy formation

The percentage of the electrons gained by each remaining ion upon oxygen vacancy formation is calculated by using the PBE+U method and shown in Fig. S7. The percentage of the electrons gained by the three elements upon oxygen removal, together with the corresponding oxygen vacancy formation energy, in the pseudocubic and orthorhombic & rhombohedral $LaMO_3$ is listed in Table S5 and S6, respectively**.**

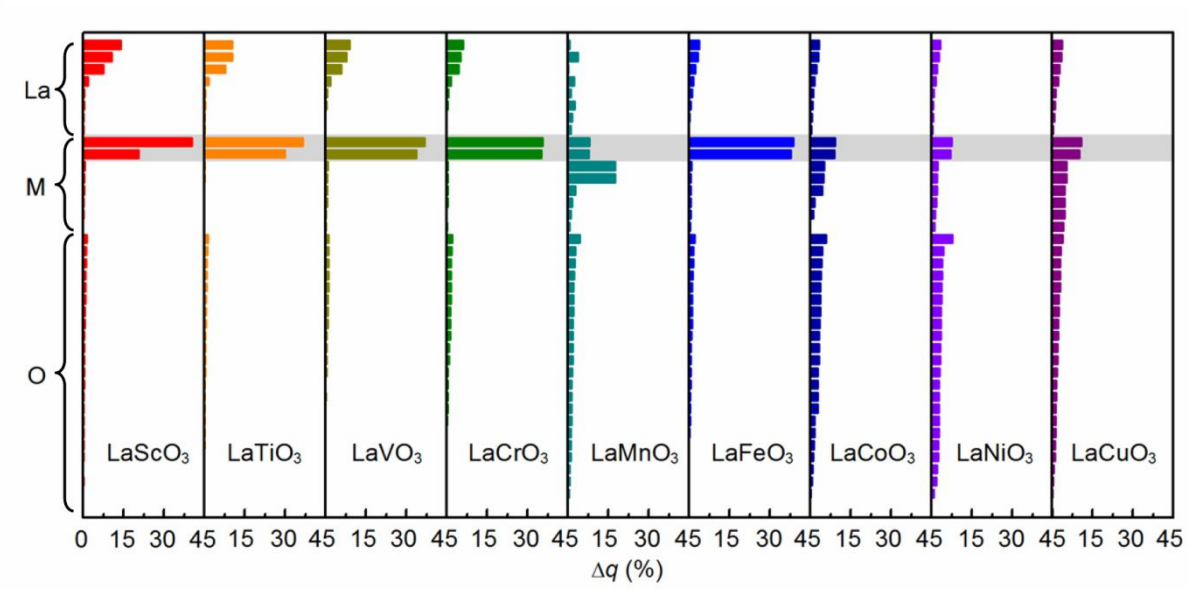

Figure S7. Percentage of the electrons gained by each remaining ion upon oxygen vacancy formation calculated by using the PBE+U method. The data for the nearest-neighbor transition metals of the oxygen vacancy are shaded in gray.

Table S5. Percentage of the electrons gained by each element in pseudocubic $LaMO_3$ upon oxygen removal.

Perovskites	BEEF-vdW+U				PBE+U			
	La	M	O	$\Delta E_{f,vac}$	La	M	O	$\Delta E_{f,vac}$
$LaScO_3$	0.32	0.64	0.04	7.07	0.33	0.61	0.06	7.10
$LaTiO_3$	0.26	0.68	0.06	6.47	0.30	0.65	0.05	6.61
$LaVO_3$	0.23	0.73	0.04	6.05	0.24	0.72	0.04	6.26
$LaCrO_3$	0.16	0.71	0.13	5.49	0.17	0.71	0.12	5.61
$LaMnO_3$	0.11	0.53	0.36	3.37	0.12	0.55	0.33	3.37
$LaFeO_3$	0.13	0.74	0.13	4.77	0.11	0.79	0.10	4.90
$LaCoO_3$	0.11	0.34	0.55	2.23	0.13	0.14	0.73	2.12
$LaNiO_3$	0.11	0.25	0.64	1.54	0.10	0.24	0.66	1.50
$LaCuO_3$	0.09	0.45	0.46	1.36	0.15	0.48	0.37	1.19

Table S6. Percentage of the electrons gained by each element in orthorhombic & rhombohedral $LaMO_3$ upon oxygen removal.

Perovskites	BEEF-vdW+U				PBE+U			
	La	M	O	$\Delta E_{f,vac}$	La	M	O	$\Delta E_{f,vac}$
$LaScO_3$	0.32	0.63	0.05	7.09	0.34	0.61	0.05	7.12
$LaTiO_3$	0.29	0.68	0.03	6.44	0.29	0.66	0.05	6.57
$LaVO_3$	0.23	0.72	0.05	6.10	0.25	0.71	0.04	6.21
$LaCrO_3$	0.16	0.71	0.13	5.42	0.16	0.71	0.13	5.54
$LaMnO_3$	0.13	0.58	0.29	3.96	0.13	0.60	0.27	3.95
$LaFeO_3$	0.12	0.73	0.15	4.74	0.10	0.77	0.13	4.79
$LaCoO_3$	0.10	0.37	0.53	2.35	0.16	0.02	0.82	2.48
$LaNiO_3$	0.14	0.25	0.61	1.49	0.12	0.23	0.65	1.44
$LaCuO_3$	0.14	0.44	0.42	1.16	0.10	0.44	0.46	1.14

10. Energy profiles for oxygen migration elementary steps in $LaMnO_3$

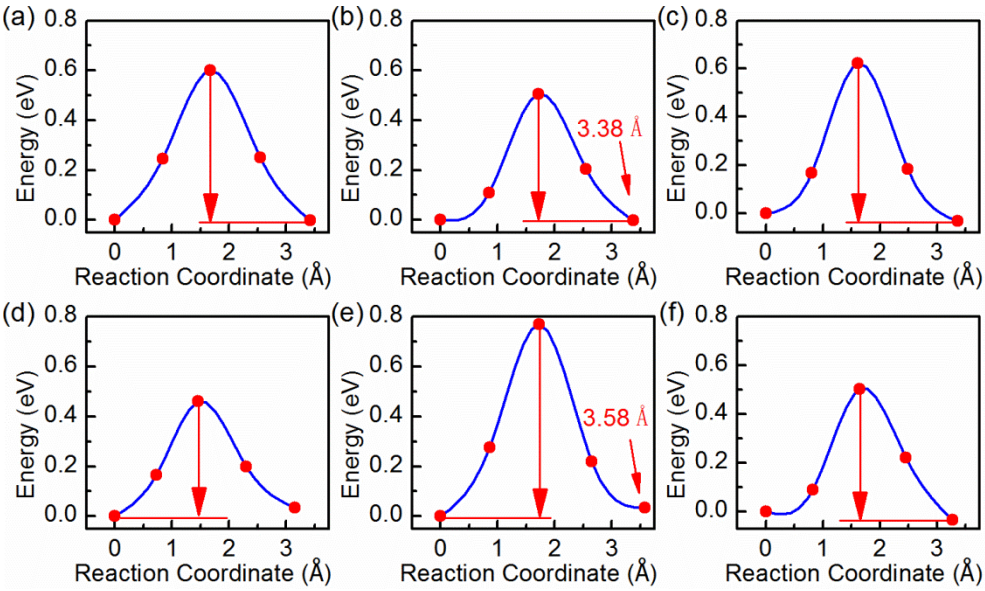

Figure S8. Energy profiles for oxygen migration elementary steps in $LaMnO_3$ calculated by using the BEEF-vdW+U method.

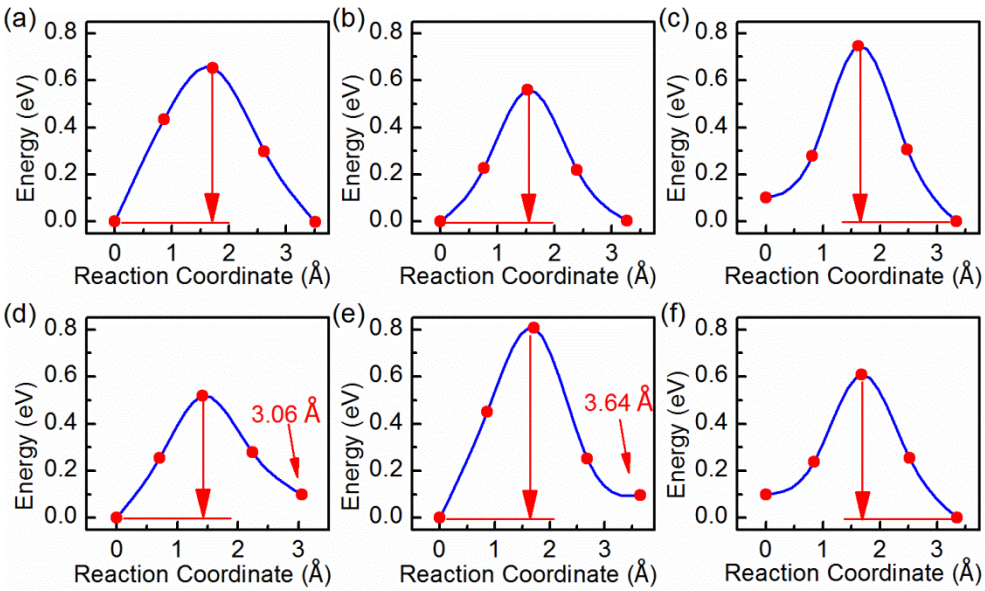

Figure S9. Energy profiles for oxygen migration elementary steps in $LaMnO_3$ calculated by using the PBE+U method.

11. Energy barriers for oxygen migration elementary steps

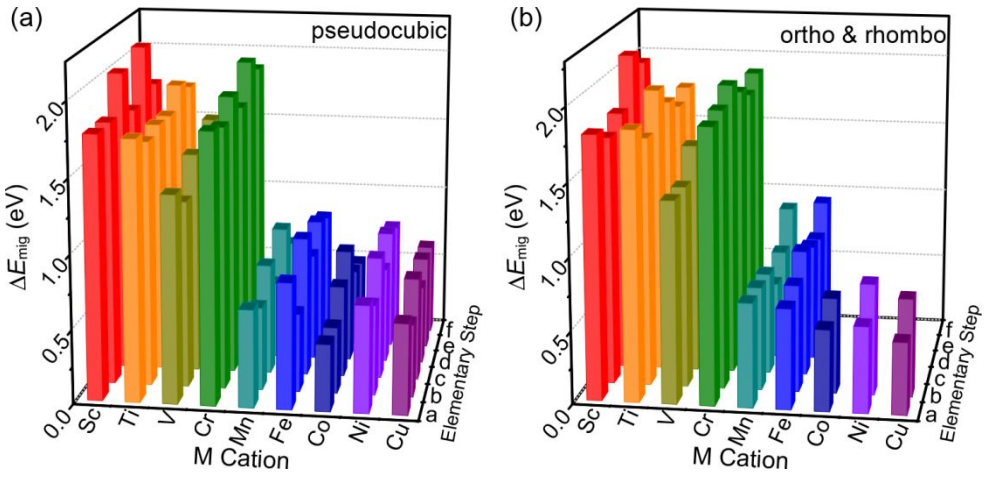

Figure S10. Calculated energy barriers (ΔE_{mig}) for oxygen migration elementary steps in the (a) pseudocubic and (b) orthorhombic & rhombohedral $LaMO_3$ (M = Sc ~ Cu) by using the PBE+U method.

12. Energy barriers for oxygen migration diffusion pathways

Table S7. Calculated energy barriers (ΔE_{mig}^{path}) for the kinetically most favorable oxygen diffusion pathways in the pseudocubic and orthorhombic & rhombohedral $LaMO_3$ by using the PBE+U method.

Perovskite	Pseudocubic		Ortho & rhomb	
	Favorable pathway	ΔE_{mig}^{path} (eV)	Favorable pathway	ΔE_{mig}^{path} (eV)
$LaScO_3$	II	1.77	II	1.70
$LaTiO_3$	II	1.65	II	1.71
$LaVO_3$	II	1.26	I	1.38
$LaCrO_3$	II	1.76	I	1.88
$LaMnO_3$	II	0.56	I	0.71
$LaFeO_3$	II	0.53	I	0.69
$LaCoO_3$	II	0.45	I	0.56
$LaNiO_3$	II	0.61	I	0.59
$LaCuO_3$	II	0.49	I	0.49

Table S8. Calculated energy barriers (ΔE_{mig}^{path}) for oxygen diffusion pathways in the pseudocubic $LaMO_3$ by using the PBE+U & BEEF-vdW+U methods.

Perovskites	PBE+U						BEEF-vdW+U					
	Ⅰ	Ⅱ	Ⅲ	Ⅳ	Ⅴ	Ⅵ	Ⅰ	Ⅱ	Ⅲ	Ⅳ	Ⅴ	Ⅵ
$LaScO_3$	1.77	1.77	1.77	2.08	2.03	2.08	1.85	1.84	1.85	2.12	2.06	2.12
$LaTiO_3$	1.75	1.65	1.75	1.81	1.69	1.81	1.61	1.57	1.61	1.80	1.62	1.80
$LaVO_3$	1.39	1.26	1.39	1.58	1.49	1.58	1.26	1.15	1.26	1.43	1.30	1.43
$LaCrO_3$	1.81	1.76	1.81	1.99	1.89	1.99	1.75	1.70	1.75	1.91	1.81	1.91
$LaMnO_3$	0.65	0.56	0.65	0.81	0.75	0.81	0.67	0.57	0.67	0.79	0.72	0.79
$LaFeO_3$	0.85	0.53	0.85	0.87	0.94	0.94	0.75	0.47	0.75	0.71	0.62	0.71
$LaCoO_3$	0.45	0.45	0.45	0.52	0.76	0.76	0.52	0.49	0.52	0.87	0.74	0.87
$LaNiO_3$	0.72	0.61	0.72	0.80	0.83	0.83	0.73	0.62	0.73	0.81	0.82	0.82
$LaCuO_3$	0.61	0.49	0.61	0.63	0.69	0.69	0.63	0.50	0.63	0.63	0.71	0.71

Table S9. Calculated energy barriers (ΔE_{mig}^{path}) for oxygen diffusion pathways in the orthorhombic & rhombohedral $LaMO_3$ by using the PBE+U & BEEF-vdW+U methods.

Perovskites	PBE+U						BEEF-vdW+U					
	Ⅰ	Ⅱ	Ⅲ	Ⅳ	Ⅴ	Ⅵ	Ⅰ	Ⅱ	Ⅲ	Ⅳ	Ⅴ	Ⅵ
$LaScO_3$	1.80	1.70	1.80	2.01	2.12	2.12	1.78	1.70	1.78	1.97	2.08	2.08
$LaTiO_3$	1.84	1.71	1.84	1.76	1.95	1.81	1.71	1.67	1.71	1.69	1.86	1.86
$LaVO_3$	1.38	1.38	1.38	1.51	1.58	1.58	1.26	1.26	1.26	1.60	1.42	1.60
$LaCrO_3$	1.88	1.91	1.91	1.88	2.01	2.01	1.82	1.86	1.86	1.82	1.92	1.92
$LaMnO_3$	0.71	0.71	0.71	0.88	0.70	0.88	0.71	0.71	0.71	0.72	0.88	0.88
$LaFeO_3$	0.69	0.74	0.74	0.94	0.87	0.94	0.56	0.68	0.68	0.73	0.73	0.73
$LaCoO_3$	0.56	0.66	0.66				0.50	0.62	0.62			
$LaNiO_3$	0.59	0.77	0.77				0.60	0.79	0.79			
$LaCuO_3$	0.49	0.68	0.68				0.49	0.67	0.67			

13. The factor determining oxygen migration barriers in $LaMO_3$

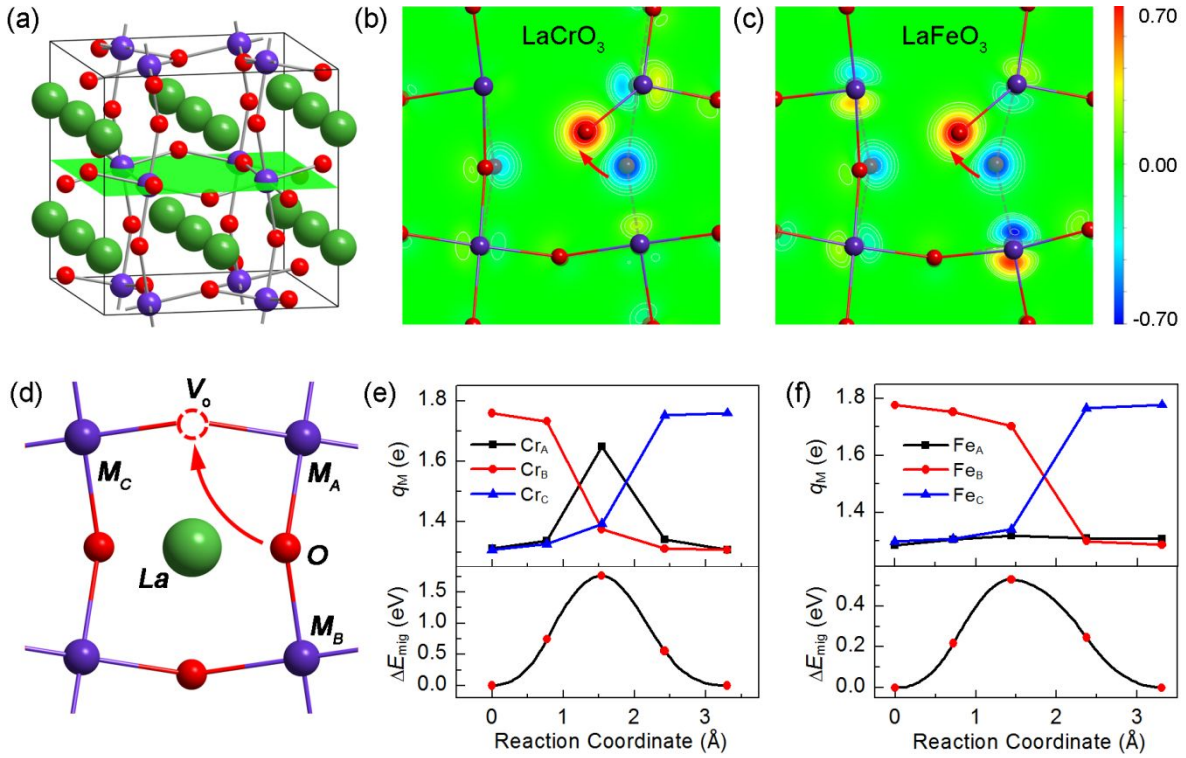

Figure S11. (a) Schematic representation of the (002) plane (shaded in green) in the pseudocubic structure; two-dimensional slices displayed along the (002) plane, showing the charge density difference between the transition and initial state for oxygen migration in (b) $LaCrO_3$ and (c) $LaFeO_3$; (d) oxygen ion migration in the (002) plane; effective Bader charges on transition metals along the MEPs for oxygen migration in (e) $LaCrO_3$ and (f) $LaFeO_3$ calculated by using the PBE+U method.

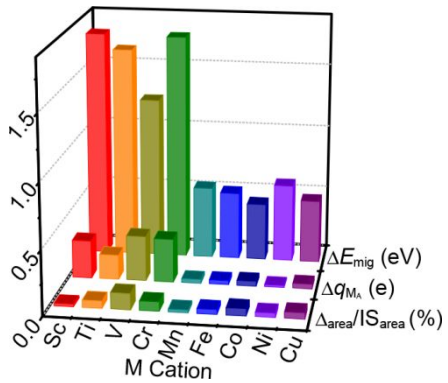

Figure S12. Relationship among the energy barrier for oxygen migration, the change (Δq_{M_A}) in the effective Bader charge on the central M_A cation from the initial state to the transition state, and the

percentage change ($\Delta_{area} / IS_{area}$) in the area of the "critical triangle" from the initial state to the transition state during the oxygen migration by using the PBE+U method.

14. The relationship between the oxygen diffusion coefficient and ΔE_{mig}^{path}

As the other component that is used to yield the diffusivity, the oxygen migration barrier is not capable of describing the variation in the diffusion coefficient.

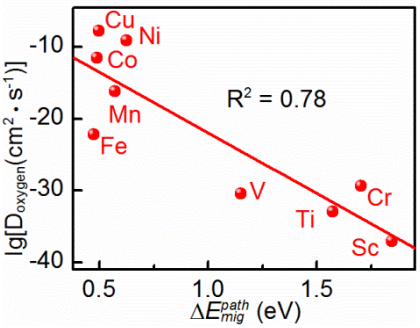

Figure S13. Dependence of the logarithm of D_{oxygen} on ΔE_{mig}^{path}.

References

(1) Afanas'ev, V. V.; Stesmans, A.; Zhao, C.; Caymax, M.; Heeg, T.; Schubert, J.; Jia, Y.; Schlom, D. G.; Lucovsky, G. Band Alignment Between (100)Si and Complex Rare Earth/Transition Metal Oxides. *Appl. Phys. Lett.* **2004,** *85*, 5917-5919.

(2) Bellakki, M. B.; Kelly, B. J.; Manivannan, V. Synthesis, Characterization, and Property Studies of (La, Ag) FeO_3 (0.0 $\leqslant$ x $\leqslant$ 0.3) Perovskites. *J Alloy. Compd.* **2010,** *489*, 64-71.

(3) Jung, J. H.; Kim, K. H.; Eom, D. J.; Noh, T. W.; Choi, E. J.; Yu, J.; Kwon, Y. S.; Chung, Y. Determination of Electronic Band Structures of $CaMnO_3$ and $LaMnO_3$ Using Optical-Conductivity Analyses. *Phys. Rev. B* **1997,** *55*, 15489-15493.

(4) Krüger, R.; Schulz, B.; Naler, S.; Rauer, R.; Budelmann, D.; Bäckström, J.; Kim, K. H.; Cheong, S. W.; Perebeinos, V.; Rübhausen, M. Orbital Ordering in $LaMnO_3$ Investigated by Resonance Raman Spectroscopy. *Phys. Rev. Lett.* **2004,** *92*, 097203.

(5) Okimoto, Y.; Katsufuji, T.; Okada, Y.; Arima, T.; Tokura, Y. Optical Spectra in (La,Y)TiO_3 Variation of Mott-Hubbard Gap Features with Change of Electron Correlation and Band Filling. *Phys. Rev. B* **1995,** *51*, 9581-9588.

(6) Saitoh, T.; Bocquet, A. E.; Mizokawa, T.; Namatame, H.; Fujimori, A.; Abbate, M.; Takeda, Y.; Takano, M. Electronic Structure of $La_{1-x}Sr_xMnO_3$ Studied by Photoemission and X-Ray-Absorption Spectroscopy. *Phys. Rev. B* **1995,** *51*, 13942-13951.

(7) Zubkov, V. G.; Bazuev, G. V.; Perelyae, V. A.; Shveikin, G. P. Magnetic Structure of $LaVO_3$. *Sov. Phys. Solid State* **1973,** *15*, 1078.

(8) Arima, T.; Tokura, Y.; Torrance, J. B. Variation of Optical Gaps in Perovskite-Type 3d Transition-Metal Oxides. *Phys. Rev. B* **1993,** *48*, 17006-17009.

(9) Bertaut, E. F.; Mareschal, J.; de Vries, G.; Aleonard, R.; Pauthenet, R.; Rebouillat, J. P.; Zarubicka, V. Etude Des Propriétés Magnétostatiques et des Structures Magnétiques des Chromites des Terres Rares et D'yttrium. *IEEE T.*

Magn. **1966,** *2*, 453-458.

(10) Elemans, J. B. A. A.; Van Laar, B.; Van Der Veen, K. R.; Loopstra, B. O. The Crystallographic and Magnetic Structures of $La_{1-x}Ba_xMn_{1-x}Me_xO_3$ (Me = Mn or Ti). *J Solid State Chem.* **1971,** *3*, 238-242.

(11) Goodenough, J. B.; Raccah, P. M. Complex vs Band Formation in Perovskite Oxides. *J Appl. Phys.* **1965,** *36*, 1031-1032.

(12) Goral, J. P.; Greedan, J. E. The Magnetic Structures of $LaTiO_3$ and $CeTiO_3$. *J Magn. Magn. Mater.* **1983,** *37*, 315-321.

(13) Hauback, B. C.; Fjellvåg, H.; Sakai, N. Effect of Nonstoichiometry on Properties of $La_{1-t}MnO_{3+\delta}$: III. Magnetic Order Studied by Powder Neutron Diffraction. *J Solid State Chem.* **1996,** *124*, 43-51.

(14) Huang, K.; Lee, H. Y.; Goodenough, J. B. Sr- and Ni- Doped $LaCoO_3$ and $LaFeO_3$ Perovskites: New Cathode Materials for Solid-Oxide Fuel Cells. *J Electrochem. Soc.* **1998,** *145*, 3220-3227.

(15) Koehler, W. C.; Wollan, E. O. Neutron-Diffraction Study of the Magnetic Properties of Perovskite-Like Compounds $LaBO_3$. *J Phys. Chem. Solids* **1957,** *2*, 100-106.

(16) Moussa, F.; Hennion, M.; Rodriguez-Carvajal, J.; Moudden, H.; Pinsard, L.; Revcolevschi, A. Spin Waves in the Antiferromagnet Perovskite $LaMnO_3$: A Neutron-Scattering Study. *Phys. Rev. B* **1996,** *54*, 15149-15155.

(17) Sakai, N.; Fjellvâg, H.; Hauback, B. C. Structural, Magnetic, and Thermal Properties of $La_{1-t}Ca_tCrO_{3-\delta}$. *J Solid State Chem.* **1996,** *121*, 202-213.

(18) Stølen, S.; Grønvold, F.; Brinks, H.; Atake, T.; Mori, H. Energetics of the Spin Transition in $LaCoO_3$. *Phys. Rev. B* **1997,** *55*, 14103-14106.

(19) Zhou, X. D.; Pederson, L. R.; Cai, Q.; Yang, J.; Scarfino, B. J.; Kim, M.; Yelon, W. B.; James, W. J.; Anderson, H. U.; Wang, C. Structural and Magnetic Properties of $LaMn_{1-x}Fe_xO_3$. *J Appl. Phys.* **2006,** *99*, 08M918.

(20) Cwik, M.; Lorenz, T.; Baier, J.; Müller, R.; André, G.; Bourée, F.; Lichtenberg, F.; Freimuth, A.; Schmitz, R.; Müller-Hartmann, E.; et al. Crystal and Magnetic Structure of $LaTiO_3$: Evidence for Nondegenerate t_{2g} Orbitals. *Phys. Rev. B* **2003,** *68*, 060401.

(21) El-Mellouhi, F.; Brothers, E. N.; Lucero, M. J.; Bulik, I. W.; Scuseria, G. E. Structural Phase Transitions of the Metal Oxide Perovskites $SrTiO_3$, $LaAlO_3$, and $LaTiO_3$ Studied with A Screened Hybrid Functional. *Phys. Rev. B* **2013,** *87*, 035107.

(22) Gavin, A. L.; Watson, G. W. Modelling the Electronic Structure of Orthorhombic $LaMnO_3$. *Solid State Ionics* **2017,** *299*, 13-17.

(23) He, J.; Franchini, C. Screened Hybrid Functional Applied to $3d^0 \rightarrow 3d^8$ Transition-metal Perovskites $LaMO_3$ (M=Sc–Cu) : Influence of the Exchange Mixing Parameter on the Structural, Electronic, and Magnetic Properties. *Phys. Rev. B* **2012,** *86*, 235117.

(24) Hong, J.; Stroppa, A.; Íñiguez, J.; Picozzi, S.; Vanderbilt, D. Spin-phonon Coupling Effects in Transition-metal Perovskites: A DFT + U and Hybrid-functional Study. *Phys. Rev. B* **2012,** *85*, 054417.

(25) Rivero, P.; Meunier, V.; Shelton, W. Electronic, Structural, and Magnetic Properties of $LaMnO_3$ Phase Transition at High Temperature. *Phys. Rev. B* **2016,** *93*, 024111.

(26) Zhang, X.-b.; Gang, F.; Wan, H.-l. Density Functional Theory Study on Spin States of $LaCoO_3$ at Room Temperature. *Chinese J Chem. Phys.* **2014,** *27*, 274-278.